LIMNOLOGY
and
OCEANOGRAPHY: METHODS

Limnol. Oceanogr.: Methods 8, 2010, 155–171

Acoustic imaging of natural gas seepage in the North Sea: Sensing bubbles controlled by variable currents

J. Schneider von Deimling[1,5], J. Greinert[2], N. R. Chapman[3], W. Rabbel[4], and P. Linke[1]

[1]Leibniz Institute of Marine Sciences (IFM-GEOMAR), Wischhofstr. 1-3, 24148 Kiel, Germany

[2]Royal Netherlands Institute for Sea Research (NIOZ), Dept. Marine Geology, P.O. Box 59, 1790 AB, Den Burg (Texel), The Netherlands

[3]Univ. of Victoria, School of Earth and Ocean Sciences, P. O. Box 3055, Victoria, BC V8W 3P6, Canada

[4]University CAU Kiel, applied geophysics, Otto-Hahn-Platz 1, 24118, Kiel, Germany

[5]now at Leibniz Institute for Baltic Sea Research Warnemünde (IOW), Seestrasse 15, 18119 Rostock, Germany

Abstract

Natural seepage from the seafloor is a worldwide phenomenon but quantitative measurements of gas release are rare, and the entire range of the dynamics of gas release in space, time, and strength remains unclear so far. To mitigate this, the hydroacoustic device GasQuant (180 kHz, multibeam) was developed to monitor the tempo-spatial variability of gas bubble releases from the seafloor. GasQuant was deployed in 2005 on the seafloor of the seep field Tommeliten (North Sea) for 36 h. This in situ approach provides much better spatial and temporal resolution of seeps than using conventional ship-born echo sounders. A total of 52 gas vents have been detected. Detailed time series analysis revealed a wide range of gas release patterns ranging from very short periodic up to 50 min long-lasting events. The bulk gas seepage in the studied area is active for more than 70% of observation time. The venting clearly exhibits tidal control showing a peak in the second quarter of the tidal pressure cycle, where pressure drops fastest. The hydroacoustic results are compared with video observations and bubble flux estimates from remotely operated vehicle dives described in the literature. An advanced approach for identifying and visualizing rising bubbles in the sea by hydroacoustics is presented in which water current data were considered. Realizing that bubbles are moved by currents helps to improve the detection of gas bubbles in the data, better discriminate bubbles against fish echoes, and to enhance the S/N ratio in the per se noisy acoustic data.

Marine methane gas seepage is a worldwide phenomenon, especially on continental margins. In shallow waters such as the North Sea, the released methane has the potential to enter the atmosphere (Rehder et al. 1998), where it acts approximately 25-fold more effectively (on a 100-y timescale) as the same amount of CO_2 in terms of its global warming potential (Lelieveld et al. 1993). Today, atmospheric methane is estimated to contribute 18% of the total atmospheric radiative forcing (Forster et al. 2007 [Intergovernmental Panel on Climate Change (IPCC) publication]).

Methane may migrate as dissolved and/or free gas phase through the sediment often following geological and sedimentological pathways and eventually escapes into the bottom water. If methane accumulates in the sediment and if the solubility in the porewater is exceeded, microbubbles may form and will further grow depending on the environmental settings as sediment characteristics, hydrostatic pressure, methane and other gas supply from below, and biogeochemical processes. At such methane rich sites, methane is often released as free gas (gas bubbles) into the water column.

Already in the 1960s, Ohle (1960) and McCartney and Bary (1965) observed that rising bubbles can be detected with high

*Corresponding author: E-mail: jens.schneider@io-warnemuende.de

Acknowledgments

The authors would like to thank our project partner L-3 Communications ELAC Nautik GmbH for technical software and hardware support, system adaption, and extensive and fruitful discussion, namely Peter Gimpel, Jörg Brockhoff, Boris Schulze, and Sven Rohde. We greatly appreciate technical work and system maintenance performed by Bernhard Bannert and Matthias Türk for lander operations. Data processing was additionally supported by GIS related work of assistant student Nina Köplin. Finally, we would like to thank the crew of RV *ALKOR* and our colleagues for their assistance during the cruises into the North Sea. This is publication Geotech-862. The *ALKOR* cruises were part of the COMET project in the framework of the R&D program GEOTECHNOLOGIEN, funded by the German Ministry of Education and Research (Grant 03G0600D).

DOI 10.4319/lom.2010.8.155

frequency active sonars (>3 kHz). Since then, bubbles rising from the sea or lake floor have often been detected by various acoustic systems such as singlebeam (Merewether et al. 1985; Hornafius et al. 1999; Artemov et al. 2007; Ostrovsky et al. 2008), multibeam (Schneider von Deimling et al. 2007; Nikolovska et al. 2008) and side-scan sonar (Klaucke et al. 2005). Because of the shape in echograms, the hydroacoustic manifestation of bubbles in the water column has been termed "flare" (e.g., Greinert et al. 2006). The drawback by using ship-mounted singlebeam echosounders for high resolution bubble release studies is the beam angle of several degrees that results in a large footprint and low ping rate both increasing with depth. The resulting limited resolution and the time needed for a detailed monitoring survey limits the use of such systems to exploration rather than high resolution monitoring tools. Nevertheless, singlebeam echosounders have demonstrated to be suited for finding bubble releasing seep areas and estimating flux and bubble sizes at single seeps (Artemov et al. 2007; Ostrovsky et al. 2008). Direct sampling and video observation of individual gas vents (the actual hole from which bubbles are released) by submersibles, ROVs, and scuba divers improved our knowledge about naturally occurring bubble size spectra (Leifer and Boles 2005a; Leifer and Boles 2006) and the relation between rising speed, bubble size, and bubble surface character (Rehder et al. 2002). Even though gas flux measurements could be conducted during several dives (Tryon et al. 2002; Sauter et al. 2006), long-term quantitative measurements (>1 d; e.g., Greinert et al. 2009) disclosing temporal variations and the response to, e.g., tidal pressure changes, are sparsely available. Most of the experiments were conducted in very shallow environment (Martens and Klump 1980; Boles et al. 2001; Leifer et al. 2004) and are technically limited considering deeper deployments such as performed with the bubbleometer described by MacDonald et al. (1994). A very good knowledge about the transient behavior of vent activity is crucial for flux estimates. If bubble venting is active during limited time periods only, the extrapolated total flux is most likely overestimated.

With respect to a possible impact on global climate, the strength of the bubble release is important. A fixed gas volume that is released as one vigorous burst over short time is more likely to enter the atmosphere than by "gentle" continuous release. The reason for this is the increased bubble rising speed due to upwelling effects, as well as slower loss by diffusion due to elevated methane concentrations in the aqueous-plume (Leifer et al. 2004). Gas ebullition is generally controlled by tides and other external pressure changing processes and thus long-term observations are needed to identify these processes.

To mitigate the limitations of vessel-mounted sonar and direct observation and sampling (submersibles, remotely operated vehicle [ROV], scuba divers, video-sled systems), the hydroacoustic lander-based monitoring system GasQuant (180 kHz) was developed by IFM-GEOMAR and L-3 ELAC Nautik in 2001 (Greinert 2008). The system is able to detect gas bubbles remotely from a great distance and does not disturb the sensible fluid flow system of the actual gas releasing seep area by its weight or the measurement itself. The 65 m range of GasQuant largely exceeds visual observation possibilities especially in muddy water and has a high resolution in space (9 cm along the beam) and time (4.4 second ping interval). Greinert (2008) gives a detailed description of the system and processing steps and shows the temporal variability of bubble release from a shelf seep site in the Black Sea. Here we present extended processing techniques and study the temporal variability of 52 individual gas vents at the Tommeliten seep area in the Central North Sea using data recoded during two RV *ALKOR* cruises in 2005 and 2006 (ALK259, ALK290). The resulting GasQuant data will serve as a base for quantitative gas flux estimates in further publications.

Materials and procedures

Bubble acoustics—The physical background of the acoustic gas bubble detection is based on the large differences in density and sound velocity between water and gas (acoustic impedance). The harmonic oscillator response at the natural frequency of a gas bubbles may additionally contribute to scattering due to the large compressibility of the gas and almost incompressible water displacement interactions. Thus gas bubbles in water act as strong reflectors/scatterers and even single gas bubbles or fish can be tracked by sonar.

The backscattering cross-section σ_{bs} of a single gas bubble is defined as

$$\sigma_{bs} = \frac{a^2}{\left[(\frac{f_{res}}{f})^2 - 1\right]^2 + \delta^2} \quad (1)$$

where a is the radius of the bubble and f_{res} its corresponding resonance frequency. f is the operating sonar frequency and δ the so-called damping constant. After Minnaert (1933), the resonance frequency of a clean gas bubble can be calculated by

$$f_{res} = \frac{1}{2\pi a}\sqrt{\frac{3\gamma P_w}{\rho_w}} \quad (2)$$

where γ is the ratio of the specific heats of bubble gas, P_w the ambient pressure, and ρ_w the water density. If the resonance frequency f_{res} of a bubble equals the transmit frequency f of the system, then the backscattering σ_{bs} peaks and the acoustic cross-section is much higher than compared to that of a rigid object of similar geometry (geometrical cross-section). In the off-resonance domain, sufficiently large bubbles cause strong backscattering (Commander and Moritz 1989). However, the scattering becomes then very directional and complicated. Instead of calculating σ_{bs} after Eq. 1, larger bubbles (compared with the wavelength) require solving the three-dimensional wave equation for the pressure field (Anderson 1950; Feuillade and Clay 1999). If a nonresonating bubble is much smaller

than the acoustic wavelength, the bubble behaves as a weak Rayleigh scatterer and—depending on the Signal to Noise ratio (*S/N*) of the system—cannot be detected.

Most hydroacoustic bubble research during the past decades was undertaken to study the acoustic response of micrometer bubbles entrained into the surface water by wind and/or ships. Here, resonance effects play a crucial role at the common operating frequencies, and quantification becomes only possible with multifrequency systems/approaches (Medwin 1977; Vagle and Farmer 1992).

In contrast, the mono-frequent GasQuant system was designed to detect bubbles in the off-resonance domain, where a linear relationship between bubble density and echo integrated intensity is expected to occur (Foote 1983). Greinert and Nützel (2004) as well as Ostrovsky et al. (2008) have shown that the backscatter increases with gas flux for bubble spectra typical for seeps and the used sonar frequencies (40–400 kHz). These results served as a base for the GasQuant system design and data interpretation. However, resonant bubbles would disturb the correlation. Visual observations in the study area and at other seepage areas around the world indicate that seep bubbles typically have a range of 1–15 mm in diameter (Hornafius et al. 1999; Rehder et al. 2002; Leifer and Boles 2005a). These sizes are well in the off-resonance domain when using the 180-kHz transducer of GasQuant in water depths down to 1000 m.

Methods—The main goal in the beginning of cruise ALK259 was to find an active gas seeping area to deploy the GasQuant system. This was undertaken by using the ship-mounted singlebeam sonar systems for flare mapping and a bathymetric multibeam system, which should give more insight in possible seepage-related morphological features and backscatter changes.

Singlebeam: A Kongsberg-Simrad EK 60 singlebeam sonar equipped with a 38 kHz transducer (SIMRAD ES 38b) was used for water column and flare imaging. The pulse length was set to 1 ms and the given opening angle along and across track is 6.5° and transforms into a circular footprint of 7.9 m at 70-m water depth. This sensitive sonar is suitable for flare imaging and operates off-resonant at the given depth and expected seep bubble radii (bubbles of 1–15 mm have a corresponding f_{res} between 9.1 and 0.6 kHz at this depth, Eq. 2). During surveys, the gain had to be adjusted to account for changing acoustic noise level so that the display is sensitive for weak echoes but not superimposed by too much noise. To reduce noise derived from the vessel, the survey speed was reduced to 3 knots. Operating with these settings resulted in the detection of many high backscatter "clouds." Only those patterns showing flarelike features as pointed out by Judd et al. (1997) and a vertical extent of at least 20 m from the bottom have been considered as bubble induced and are plotted in Fig. 1 as seep position. Localizing all recorded flares and determination of their height and intensity was completed through post processing using the MYRIAX ECHOVIEW software.

Multibeam mapping: Prior to the cruise, we installed the shallow water swath multibeam system SEABEAM 1180 (L-3 ELAC Nautik 2003) on RV *ALKOR*. This 180 kHz system covers a 153° swath angle. The horizontal resolution at 70-m water depth is about 3.7 m; the vertical resolution is estimated to be better than 0.45 m (0.5% of the water depth). Motion compensation was achieved by using an IXSEA Octans 3000 motion reference unit. A sound velocity probe was mounted next to the transducers to guarantee correctness of sound velocity values during the beamforming. Sound velocity profiles were processed from conductivity–temperature–depth (CTD) data for exact depth calculation. At a fairly flat and featureless area, the system was calibrated for roll offset.

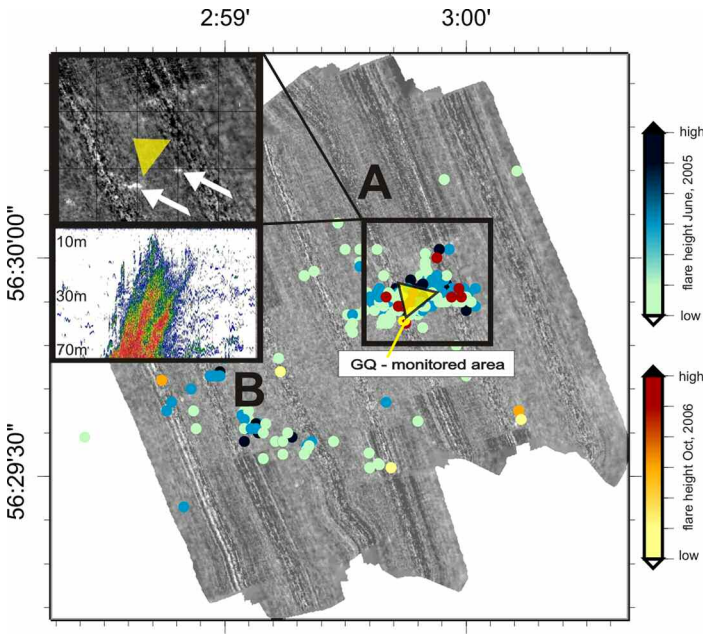

Fig. 1. Overview map of detected gas flares. Each colored point represents a flare (subplot) recorded with the EK 60 (38 kHz) sounder in 2005 (bluish) and 2006 (reddish). The flares have been classified into low, medium, and high depending on their rising height above the seafloor (<20 m absf: low; 21–40 m: medium; >40 m: high). The GasQuant monitored area is indicated as a yellow triangle in the center of the flare cluster A. The grayscale color coded background represents backscatter intensity from multibeam survey. A few patches of higher backscatter (white arrows, upper left subplot) are present.

GasQuant: On the ALK259 cruise, GasQuant was the most important acoustic device to monitor temporal and spatial variation of gas release. It is composed of an adapted ELAC SEABEAM 1000 multibeam electronic, a 180 kHz transducer, and a data storage and system control PC (Greinert 2008). The device is mounted in a lander system (Pfannkuche and Linke 2003) and deployed video guided with the transducer facing into the direction of the targeted seep area. The cardanically fixed transducer is placed about 3 m above the seafloor and produces a swath of 63° horizontally consisting of 21 beams with 3° by 3° beam angle each. The swath covers a range between 13 and 63 m from the transducer resulting in a 2075 m^2 large area (Fig. 2).

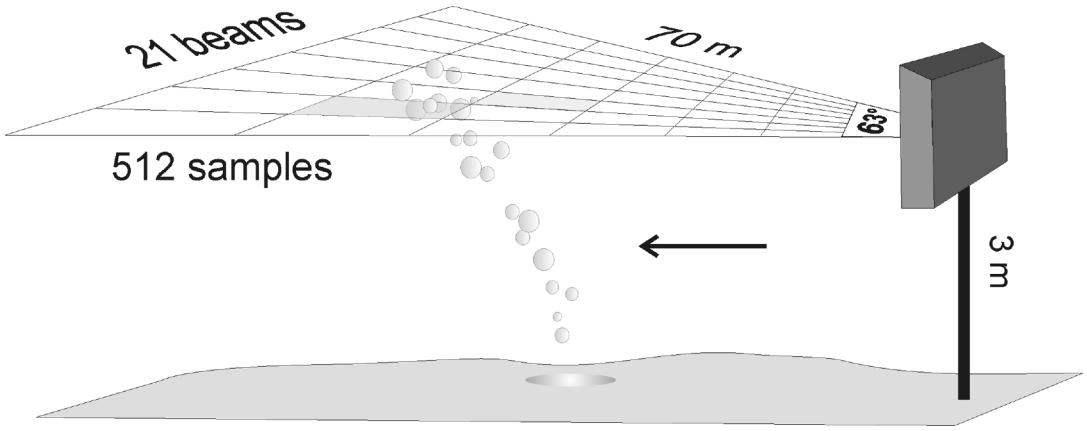

Fig. 2. Schematic sketch of the deployed transducer insonifying a bubble chain. The swath covers a range of 60 m and echo time series is divided into 512 samples. Each beam is 3° wide and the overall swath width of all 21 beams is 63°.

In operational mode, GasQuant transmits a 0.150-ms long acoustic pulse (corresponding to 0.225 m at 1500 m/s) and receives a time series of the echo-envelope for each of the 21 beams. If a single gas bubble or bubble cloud rises from the seafloor into the acoustic swath, the high backscattering leads to enhanced echo level at the transducer. Although the system corrects the received echoes for geometrical spreading and absorption using a time-varying gain (TVG), the resulting echoes represent uncalibrated values due to missing knowledge about exact transmission source level and transduction effectivity. Therefore, quantitative analysis of echo levels is not feasible at this stage of development. Finally, the system performs echo integration to generate a system specific db envelope value of 8-bit (0-255), which is termed "GasQuant echo level" ("GQEL") in the following.

Compared with a standard multibeam mapping system, which is optimized for bottom detection, the GasQuant electronic system was adapted to sequentially scan the water column. For each beam, the received envelope of the signal is converted from analogue to digital every 128 µs resulting in 512 samples along the transducer's view (Fig. 2).

Hovland and Judd (1988) report a typical bubble diameter of 10 mm for the working area and a corresponding bubble rise speed is expected to range around 20 cm/s (Clift et al. 1978). A complete scan of the entire swath needs about 4.4 s and thus we can be sure that each bubble is at least insonified once when passing the swath of 3° angle (–3 dB). The resulting data set consists of 512 × 21 time series ("traces") of enveloped backscatter values.

During an experimental setup (Fig. 3), the system sensitivity was tested with respect to bubble size and flux rate in a similar way as outlined in Greinert and Nützel (2004). Even low fluxes of only 0.2 L/min and bubbles with a diameter of only 2 mm were clearly recognized as elevated GQEL values in the data. With increasing gas flux and number of insonified bubbles, the GQEL values increased.

Current measurements: In addition to the GasQuant system, another lander equipped with an upward looking Acoustic Doppler Current Profiler (ADCP) (2 MHz Nortek Aquadopp Profiler) was simultaneously deployed in the nearby bubble-free environment (DOS 1, 56°30.00 N, 2°59.62 E) next to the GasQuant system. The ADCP measured the water velocity and changes in volume backscattering strength *Sv* that were both supplied by data export using the *ExploreP* software of NORTEK.

Pressure measurements: A CTD (SBE 25) was fixed to the GasQuant lander to monitor environmental changes and particularly link tidal pressure changes to the observed gas release patterns. All data sets were synchronized by setting all devices to Middle European Summer Time (MESZ) [= Coordinated Universal Time (UTC) + 2] prior to the deployment.

GasQuant data processing using water current information—The GasQuant data volume that is acquired during several days of deployment grows large, and various sources of noise close to the 180 kHz band perturbs the data (system self-noise, engine/hydrolic pumps, thermal noise, biologic scatter). This, together with the fundamental aim of detecting bubble release events in the data, requires postprocessing. A key feature during postprocessing was to consider current velocity effects on the bubbles while rising through the acoustic swath. The current-induced shifting of bubbles in the acoustic swath of GasQuant is controlled by the sum of the vertical buoyancy and mainly horizontal water current velocity vectors. If bubbles are emanating from a vent, they become laterally shifted, and if currents change direction and/or speed, successive bubbles pass the swath at adjacent cells. As a result, bubbles from one vent are recognized in several cells of one beam and might even move between beams. During the GasQuant experiment, simultaneous ADCP measurements reveal a significant tidal impact on the current (Fig. 4). Consequently, a displacement of bubbles is expected to occur also on a tidal base. The magnitude of this displacement can be easily estimated; e.g., a bubble of 10 mm

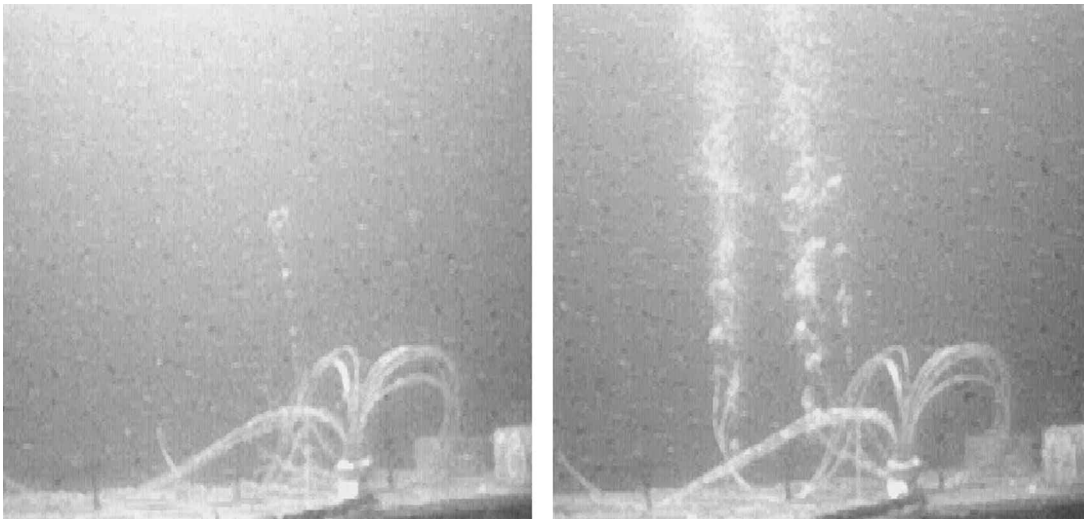

Fig. 3. GasQuant sensitivity test assembly, where an artificial seep area was set up in a ships dock. Low (left) to medium (right) gas flux rates of 0.2 L and 5 L per min could be generated. Simultaneously, GasQuant insonified these bubbles and recorded backscatter data.

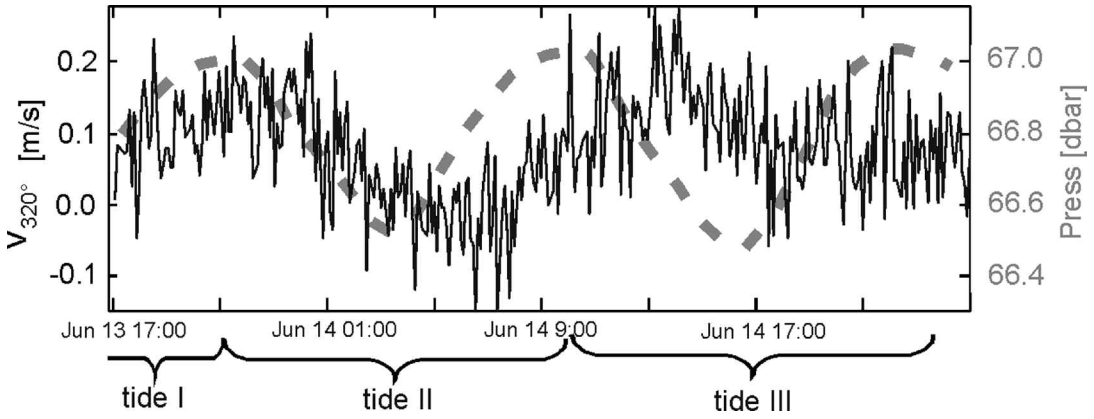

Fig. 4. Combined plot showing ADCP velocity component along track of the transducer's view direction toward NNW (N positive, S negative) together with CTD pressure data (dashed line) gathered during the GasQuant deployment. The entire deployment time is separated into three sections termed "tide I," "tide II," and "tide III" with respect to the differing tidal cycles.

diameter has a terminal rising velocity v_z of approximately 20 cm/s (Clift et al. 1978) and enters the acoustic main lobe at d = 3 m above the seafloor after 15 s rise time (t_{up}). Using the horizontal velocity components (v_h) from ADCP measurements the expected horizontal bubble displacement *bd* at d results in:

$$bd(d) = v_h \times t_{up} \quad (3)$$

This displacement of bubbles can be visualized in trace plots, which show backscatter amplitude time series (traces) of adjacent cells being drawn underneath each other. Fig. 5 shows both the predicted bubble displacement (solid sinusoidal line) and the real displacement given as the tide-caused sinusoidal curvelike pattern. As long as such curves are clearly separated from each other, each curve is considered to be caused by one vent. This is even valid for noncontinuous bubble release as long as its repetition rate is high enough to trace the sinusoidal pattern. The predicted and measured displacement curves agree particularly well, and this similarity can be regarded as an unambiguous indication for rising gas bubbles in swath plots. This bubble detection method works best if the transducers view is orientated parallel to the maximum current changes. Tidal effects occur in all marine environment and at least small current shifts are likely, even in deep water. Considering the high along-track resolution (9 cm) only weak current changes are required to cause a measureable bubble displacement in 3 m above the bottom that are easily picked up as sinusoidal pattern during our 36-h long-term monitoring. Automatic event detection algorithms such as correlation processing (Dworski and Jackson 1994) or "short/long term averaging" (STA/LTA) known from seismic processing have been considered and rejected, because the visual bubble pat-

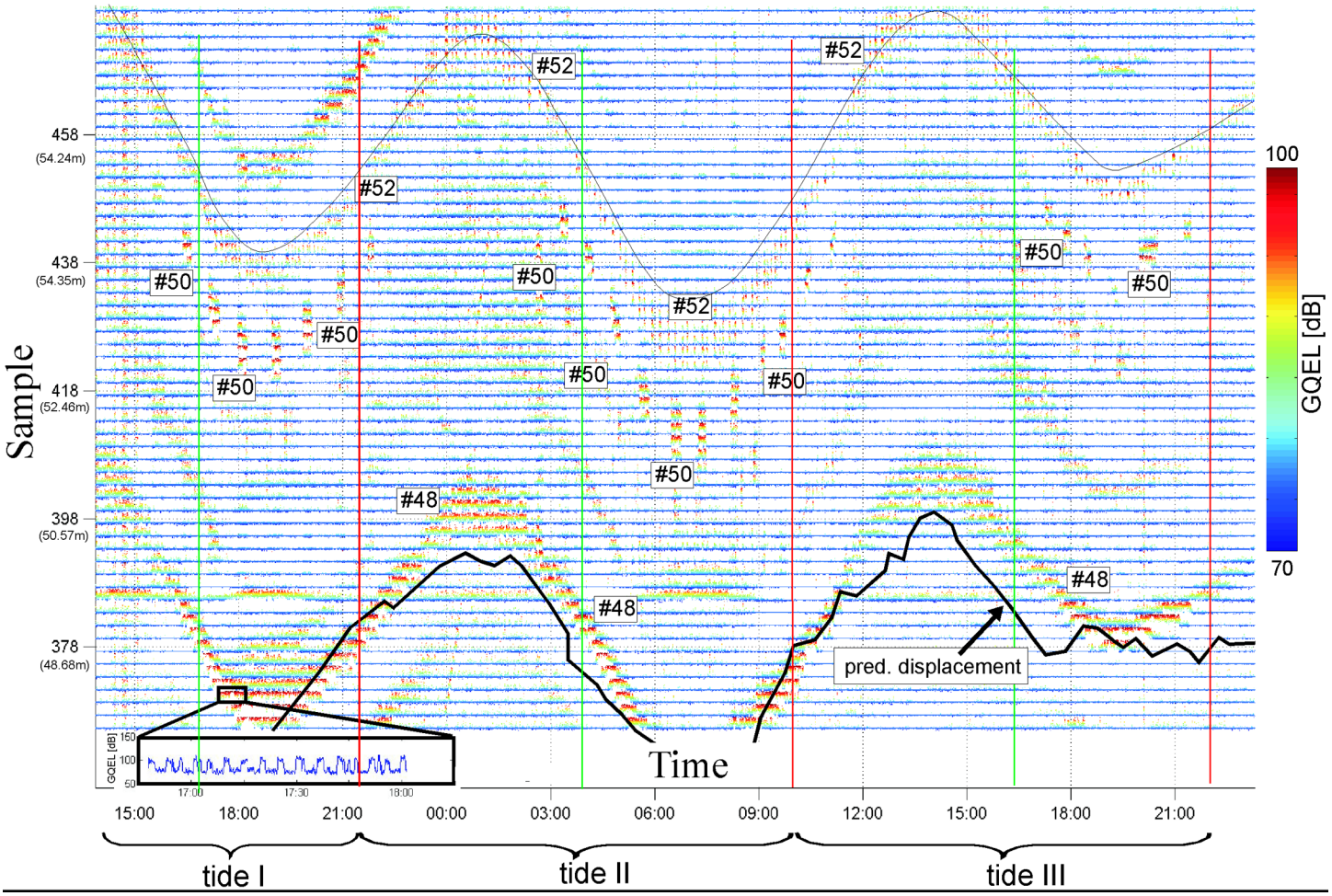

Fig. 5. GasQuant data set showing 60 traces of beam number 1 corresponding to the very outer left beam (Fig. 2). The traces originate from adjacent samples labeled on the *y* axis by sample number and distance to transducer (meter). Color-coded time series values correspond to GasQuant GQEL values (color bar). The entire time series comprises 36 h where vertical green and red lines indicate moment of minimum and maximum water level, respectively. The thin black sinusoidal retraces vent #52 and the thick sinusoidal line represents the predicted bubble displacement derived from ADCP data. An enlarged subplot presentation in the lower left corner stresses underlying higher gas release frequencies that vanish in the bulk presentation due to print/pixel resolution. pred., predicted.

tern recognition works much quicker and more reliably against erroneous interpretation.

Nomenclature: To assist the following data description, some data types and terms need to be introduced that follow in wide parts the definitions given by Greinert (2008). We define a three-dimensional matrix composed of GQEL values (GasQuant echo level in dB) where the first spatial dimension is along the transducer's view (along the samples of the given beam, Fig. 2), which is called the "sample-index *s*" (1–512). Across track, from one beam to the other, is the beam direction with beam-index *b* (1–21). The time in seconds is the third dimension abbreviated by index *t* (1–29000). Each point of this matrix holds the backscatter value measured at a certain time at a certain spot in the hydroacoustic swath. Holding *s* and *b* fixed equals choosing one cell and its corresponding $trace_{s,b,1\text{-}29000}$. A subset of this time series, e.g., $trace_{s,b,t1\text{-}t200}$ is termed a "sniplet." To analyze the activity of one vent rather than the activity of a GasQuant cell (fixed *s* and *b*), those neighboring cells have to be merged that show or could have shown higher backscatter caused by bubbles. Adding all those sniplets results in a "stacked trace." This is different to the definition in Greinert (2008) who stacked (added) entire traces and not only those parts which could, or actually contain, bubble reflections based on the current induced bubble displacement.

To decide whether an elevated backscatter signal is regarded to be caused by free gas or reverberation, a detection threshold in dB has to be set. Values above this detection threshold are considered as active time of the vent (bubbles are released), values below or at this threshold are considered as inactive time and are termed "silent." Both, active and silent times are measured in seconds and the entire active bubble release event is called a "burst." The added-up time of all bursts from one

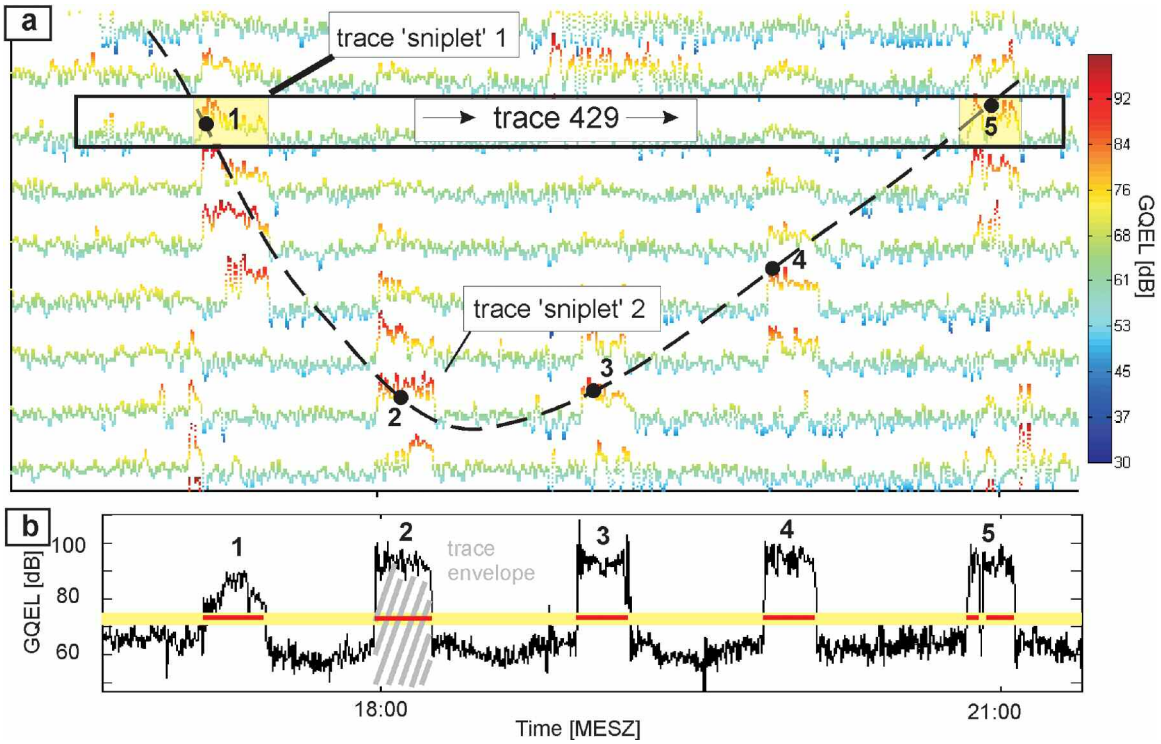

Fig. 6. (a) Trace subplot from Fig. 5 (tide I) showing five successive bubble bursts of vent #50 (labeled incrementally 1–5). The yellow rectangles within trace 429 highlight relative short active periods of the single trace 429. Enhanced signal strength can be tracked by following the splined curve (dashed line). Yellowish and reddish line segments in the vicinity of the black line are considered a signal, whereas bluish and greenish data are considered silent. (b) Stacked trace representation of picked samples from (a). The yellow line represents the color coded detection threshold (compare color bar in [a]). The seep intensity of one bubble burst plots as a gray-shaded area at burst number 2 (1800 MESZ).

vent is called "total activity time" and is again measured in seconds. Integration of GQEL values over a burst yields the seep intensity in dB × seconds. The sum of the seep intensity of all bursts from one vent represents the total seep intensity.

The compiled presentation of many traces in trace plots is preferred for simultaneous visualization of large data sets and bubble detection (Fig. 5), whereas inspection of stacked traces allows analyzing the distribution of active times, the total activity, or the seep intensity.

Filtering: To increase the *S/N* of the GasQuant data and to delete system related spikes, low pass filtering was applied. Physical parameters such as the range dependent vertical swath width $sw(d)$ and the bubble rising speed v_{up} were considered to design an effective filter. With increasing distance d of a bubble to the transducer (due to the fixed beam width of 3°), the crossing of the swath height takes increasingly more time and consequently one rising bubble is insonified increasingly more often during its ascent at larger distance from the transducer. For instance, in 50-m distance from the transducer, the vertical swath is 2.6 m wide. A typical bubble with 20 cm/s ascent rate (~10 mm diameter) needs 13 s to cross the swath.

The expected backscattering strength of a bubble should first steadily increase while entering the acoustic lobe, then peak when passing the main lobe and decrease again with further bubble ascent. Significant backscatter undulation within this ascent period can be considered as noise. This was suppressed by a 20th order low-pass Butterworth filter, designed and adapted for the changing swath geometry with $[sw(d)/v_{up}]^{-1}$ being a cutoff frequency criterion.

The raw data also contained random spikes that result in a very broad power spectrum making the above-mentioned low-pass filter ineffective for their removal. Thus, before applying the low-pass filter, a lower and upper intensity threshold was assigned to detect the spikes by logical treatment. The detected values were replaced by the mode value of a 21 samples wide window around the values that had to be replaced.

Seep detection and analysis: Trace plots show that bubbles passing the swath are recognized as sinusoidal curvelike patterns of elevated trace amplitude over time. This visual pattern recognition technique is very quick and reliable in terms of finding more or less constant bubble release in the large amount of GasQuant data. However, for computational data analysis, e.g., the determination of the total active time or seep intensity, the detection threshold is necessary to separate silent from active periods. To account for the spatial variations of background noise and changes of the noise level between different swath cells, the detection threshold was individually set for different cells. The detection threshold was set by adding twice the standard deviation to the local background value defined by the mode value calculated from the entire

trace. This was feasible, because even continuous seepage appears as relatively short sniplets, which makes mode filtering effective to determine the local background value for each trace (Fig. 5, 6a). The result of applying this computed detection threshold to detect bubble burst events matches the visual identification very well. In Fig. 6a, bubble bursts plot with yellowish/reddish points ranging from 73 to 90 GQEL. Consequently, the detection threshold was set to 73, and values below are considered as noise. We only found minor differences between statistical and visual determined threshold levels, nevertheless the impact of small deviation have been acknowledged by adding/subtracting 10% of the detection threshold. In most cases, such threshold modifications show hardly any effect on the calculated activity time (e.g., Fig. 6). Only in a few very noisy stacked traces, a variation of up to 12% in the activity time was found. However, decreasing or increasing the threshold has an immediate impact on the integrated seep intensity value, and, for later presentations the unchanged detection threshold was selected.

Stacking of traces: To obtain a complete time series that represents the total activity time of one vent, time series values from different cells have to be merged to a stacked trace. This is to include all those cells that are influenced by bubbles from one vent, but also excluding signals from adjacent vents. Thus, the sinusoidal curvelike patterns consisting of elevated backscatter values were manually digitized (Fig. 6a, black points *1–5*) and splined (Akima spline) to get a continuous time series containing the displacement of the bubbles over time. The final stacked trace (Fig. 6b) is computed by merging of time series values along this splined curve.

Bubble bursts are at least detected in three adjacent cells/traces (Fig. 6a). This is given due to the slight oversampling effect of the transmitted 0.150 ms long pulse with regard to the sample rate of 0.128 ms (Greinert 2008). In addition, the spatial dispersion of bubbles some meters above the seafloor may cause more neighboring cells to inherit similar backscatter patterns. To account for the oversampling and bubble spreading, three traces were added (stacked), one above and one below the splined sinusoidal displacement curve [$stacked\ trace = (trace_{n-1} + trace_n + trace_{n+1})/3,\ n \in (2, 511)$].

This processing was accomplished with a self-written MATLAB GUI capable to digitize the sinusoidal curvelike pattern (Fig. 6a, black spline) and to extract the requested data (Fig. 6b). Compared with previously suggested processing by Greinert (2008) who stacked entire traces, this advanced stacking technique is needed because of the small distance between single vents at Tommeliten and the considerable current variations. Without, backscatter data of bursts from neighboring vents would have been merged. Moreover the selection of active areas only improves the *S/N* of the resulting stacked trace.

Spectral analysis: To identify and quantify periodicities in the data, the stacked traces were transformed into the frequency domain using a Fast Fourier Transform (FFT) run in MATLAB. This algorithm uses zero-padding and to prevent potential leakage effects, some time series were cut down in length to exponential to the base 2. The FFT was run using a Hamming window to avoid spectral leakage caused by edges of the time series. Long-term trends in the data were removed using the MATLAB built in function "detrend." Finally the frequency content was displayed as a power spectrum.

Study area

The study area Tommeliten is located in the Greater Ekofisk area (Central North Sea, Norwegian Block 1/9) over three buried salt diapir structures that are covered by Mesozoic and Quaternary sandy and clay-rich sediments (Hovland and Judd 1988). A seismic section reveals a gas chimney (D'heur 1984) rising along a fault providing the pathway for the gas migration into the surficial clay-rich layers and locally into the water column (Hovland and Judd 1988). The topmost sediment layers have been investigated by vibro-coring and four different sediment horizons have been identified (Niemann et al. 2005). The lowest (350–240 cm below seafloor [bsf]) consists of stiff marl followed by a gassy layer of clay-silt with supersaturated CH_4 concentration (240–175 cm bsf). On top two sandy layers with and without carbonate—depending on locality—occur.

During a routine seismic survey in 1978, 3.5 kHz pinger data revealed both flarelike features in the water column and acoustic turbidity indicating gas in water and sediments (Judd and Hovland 2007). Early ROV expeditions in 1983 revealed seeps on a plain, sandy seabed with only occasional signs of biological activity (Hovland and Sommerville 1985; Hovland and Judd 1988). Those include reef-like structures locally arising in the form of small bioherms extending a few meters in diameter. Most of the gas vents have been found to be surrounded with 20-cm funnel-shaped depressions in the sandy environment.

The vents typically release bubbles from a circular 10-mm diameter hole in sandy sediments. The release of the approximately 10 mm diameter bubbles was estimated to be more or less constant with an average production rate of one bubble every 6 s. Noteworthy is an experiment documented in Hovland and Sommerville (1985) where one gas-releasing hole was filled up with sand. After about 1.5 min, the bubble stream was reestablished from this hole. The same area was resurveyed 15 y later and Hovland (2002) reports (a) new incipient seeps, (b) bacterial mats (probably *Beggiatoa* sp.), and (c) authigenic carbonate cemented bioherm structures.

Assessment

Flare distribution—Most of the time during ALK259, the water column was monitored by the EK60 singlebeam echosounder and flares were mainly concentrated in two areas (Fig. 1, blue dots). To eliminate survey artifact, only those flares recorded during the combined multibeam/singlebeam survey during ALK290 (survey was performed with uniformly distributed coverage) are plotted in Fig. 1 (red dots). They plot very similar as the distribution of all flare sites discovered (Fig. 1, blue dots). Flare cluster *A* and *B* are considered the

most intense gas-emanating areas. These findings confirm the gas seepage occurrences presented by Hovland and Sommerville (1985) and Niemann et al. (2005) but additionally stress the generally clustered nature.

GasQuant measurements—GasQuant was deployed looking northwards within the center of the most intense seepage area *A* for a total of 36 h (Fig. 1: 56°29.89′N, 2°59.80′E). After recovery, the GasQuant data set was processed and visualized on large paper printouts. Supported by the respective current velocity data (ADCP) and predicted bubble paths, a total of 52 gas vents were located in trace plots (Fig. 5). A CTD cast within the working area revealed an in situ temperature of 6.5°C at the depth and salinity of 33 psu. Based on these data, a sound velocity of 1475 m was calculated for 80 decibars (dbar) after Fofonoff and Millard (1983) to provide precise distance of samples to the transducer (Fig. 5, *y* axis).

In the following, these processing steps are illustrated and the behavior of individual vents is studied. We demonstrate GasQuant's potential to not only detect single vents, but also to reveal their small-scale temporal and spatial variability. Because of the great amount of vents detected, we only show some of them in detail. Finally, the bulk behavior of the entire seep area is described based on the GasQuant data.

Individual gas escape behavior: In Figs. 5 and 6, GasQuant data are visualized as trace plots and various release characteristics can be studied. To stress the relation to pressure changes, the in situ minimum and maximum CTD pressure (Fig. 4) are also shown in Fig. 5 (vertical lines). Redrawing elevated backscatter signals of vent #48 in Fig. 5 reveals a sinusoidal continuous curvelike pattern that is interpreted as "continuous" gas release from a single vent. A replicate but much weaker representation of this line plots 9 samples later. This is considered a "ghost" signal caused from multipath effects, where echoes from vent #48 bubbles travel not directly back to the sonar, but first hit the sandy seafloor to be received by the transducer 1.2 ms later.

Zooming into the time axis of vent #48 reveals that this vent is not really constantly active but shows short silent periods of 3 to 5 min (Fig. 5 subplot).Vent #50 and #52 exhibit a more periodic gas release still showing the same current-driven displacement as vent #48. During the first tidal cycle (*see* tide I), #52 releases gas bubbles approximately every 3 to 5 min until the beginning of tide II (23:30), where the gas release abruptly slows down to occur every 12 min.

Vent #50 exhibits much longer gas escape periods with systematic linkage to the tides. Around low tide, minimum (*see* tide I, green line) gas release begins with a 15-min long burst, followed by several bursts of the same length, with silent periods of 60 min in between. At 2130 MESZ (*see* tide I), this vent turns completely silent until begin of the next low tide phase (*see* tide II) at 0345 MESZ. Afterward, this scheme repeats almost identically, whereas at tide III an exceptional long silent period of 90 min starts around 1900 MESZ, interrupting the previous scheme; it is followed by a longer bubble burst lasting 30 min. Although #50 and #52 are separated by only 1.9 m, their transient release is not correlated to each other.

A compilation of different release patterns is shown in Fig. 7. Vent #25 releases bubbles every 5 to 6 min in bursts lasting for 3 to 4 min. These events show the typical bubble burst shape with distinct on and offset edges. This escape pattern remains active over the entire deployment time. During low tide (*see* tide II), vent #3 reveals a constant release between 0400 and 0600 MESZ but turns periodic at 0800 MESZ toward high tide. Burst lengths range between 2 and 5 min, and each burst is followed by 2 min of no release. With successive tidal cycles, this sequence recurs. Such a transitional gas release pattern was also found at vent #38 where with increasing tidal pressure the gas release turns from constant to irregular (0730 MESZ). The burst lengths range between 5 and 35 min separated by silent intervals of 2 and 15 min. Such an unsteady and pulsing gas escape pattern was additionally observed at #43 and #56.

The most prominent tidal control appears at vent #33, where gas is exclusively released during low tide (Fig. 7, Fig. 8). The gas release starts before low tide with relatively long bursts (Fig. 8a,b) of 4 min. Subsequently, the GQEL (Fig. 8a) and the length of the bursts (Fig. 8b) decline and the gas release totally vanishes around high tide. At the following tidal cycles, this release pattern repeats. The neighboring vent #34 (Fig. 8c,d) is tidally triggered as well, but exhibits only one period of several bursts during high tide. Overall, it was found that only 1% of all discovered vents exhibit an on–off tidal control (i.e., vent is active exclusively during low tide).

Spectral analysis of individual vents: To quantify the bubble release periodicities and also to overcome the high amount of data (t_1-t_{29000}) and limited trace plot resolution, FFT analyses were performed to resolve the periodicities that cannot be quantified visually. Combined plots (Fig. 9) including time series and spectral presentation of vent #25, #50, and #52 reveal minimum (a), maximum (b), and intermediate (c) gas release periodicities.

Long, tide-controlled fluctuations can be observed for vent #25 (Fig. 9a). Here, the backscatter amplitude gradually increases after passing the low water level. These higher values are considered to be caused from enhanced bubble release and they persist until reaching water level maximum and subsequently drop down to silent values. This cycle repeats during all tidal periods. This obviously tide-controlled oscillation shows up as a minor peak in the frequency domain (arrow in Fig. 9a). A secondary pronounced peak at 5 minutes occurs additionally in this spectrum. When zooming into the stacked traces very persistent bubble bursts of 5 minutes duration become visible (similar to subplot in Fig. 5).

A very distinct 50-minute period of vent #50 can be detected in both, its time and spectral domain (Fig. 9b) and confirms previous visual impressions of long bubble bursts drawn from Fig. 5. A solitary peak in the frequency spectrum indicates that concurrent frequencies besides the 50 minutes peak do not exist at vent #50.

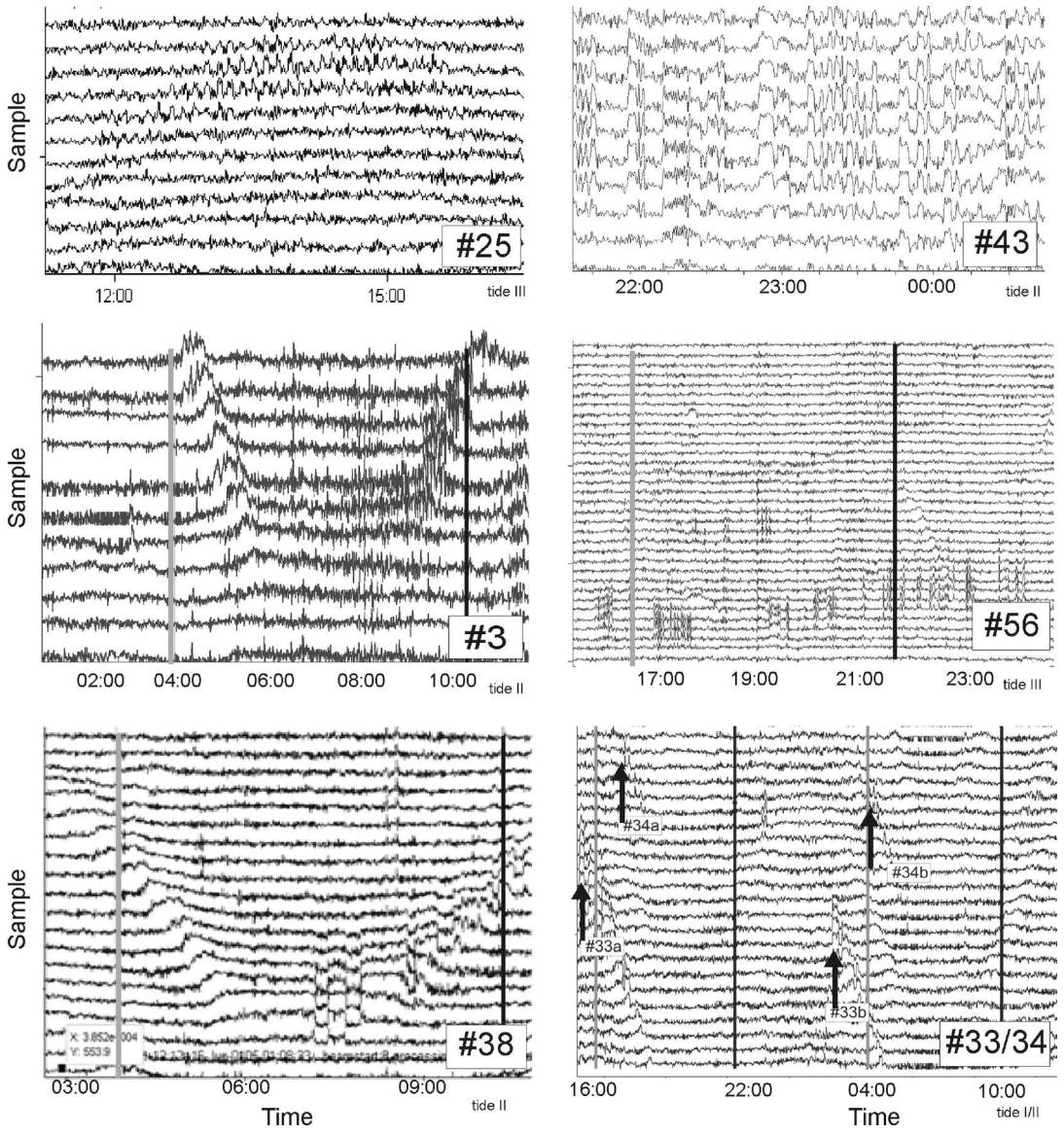

Fig. 7. Compilation of various gas escape patterns occurring at seep number #25, #43, #3, #56, #38, and #33 and #34. Note the differing time-scales and tidal phase in each subplot. Vertical black and gray lines indicate maximum and minimum water level, respectively. Additionally, tidal control of gas seepages is indicated by arrows.

The entire GasQuant data set was examined for preferential release frequencies by FFT analysis, and 18% of all seeps exhibit profound release frequencies in the range between 5 and 50 min. In addition, potential dependency of gas release frequency on tidal pressure phase was tested by computing several spectrograms but no systematic pattern between gas release and time/tidal phase could be found.

Areawide gas release behavior: GasQuant allows to exactly localize each gas-releasing vent relative to the GasQuant lander (Fig. 10). The spatial distribution of the gas vents appears homogeneously distributed in the monitored area. Enhanced along compared with across-beam resolution causes local vent clusters to appear aligned into the direction of the beam, even if the true vent cluster extent was not aligned. This is an artifact of the "limited" horizontal resolution (a too wide beam width) of the system.

A histogram of total activity time (Fig. 11a) of all vents demonstrates that the majority of vents emanate gas continuously (meaning for more than 70% of the observation time, *see* Table 1), whereas transient venting only marginally contributes to the total activity time (Fig. 11a). In terms of total seep intensity, less intense gas venting clearly dominates and only a few, rare stronger bursts occur (Fig. 11b). Such skewed distributions resemble a lognormal distribution that often occurs in natural systems and has already been mentioned in

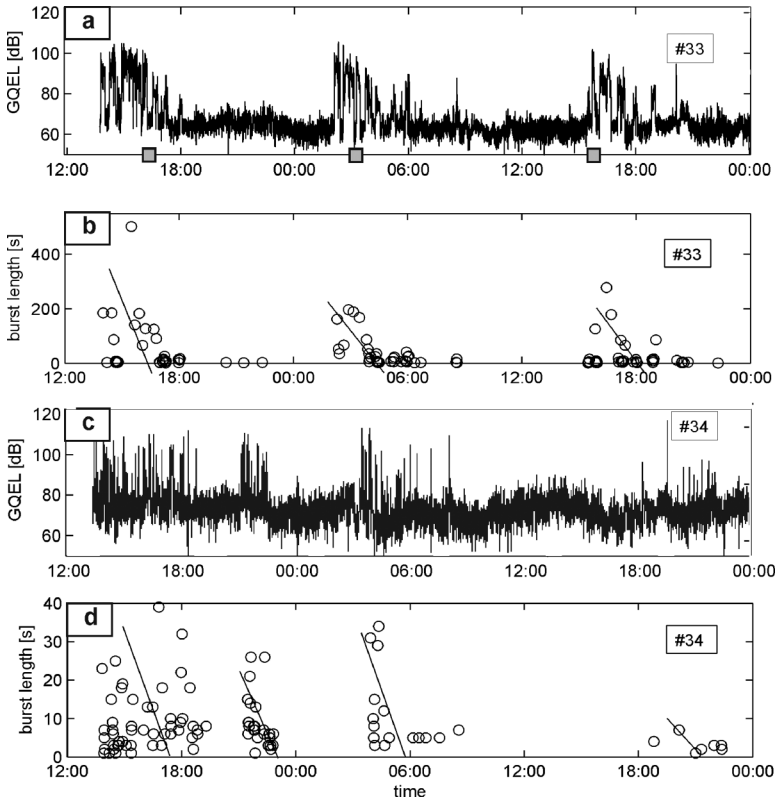

Fig. 8. (a) Stacked trace plot of seep number #33 (compare Fig. 7) showing distinct increase of GQEL attributed to enhanced gas release occurring around minimum pressure (gray square on time axis). (b) Length (seconds) of individual bubble bursts plotted versus time. Longest bursts occur at the beginning of active period and gradually decrease toward the silent period. (c) and (d) are similar to (a) and (b), but at 2200 MESZ a bubble burst of seep number #34 emanates at high tide around 2200 MESZ.

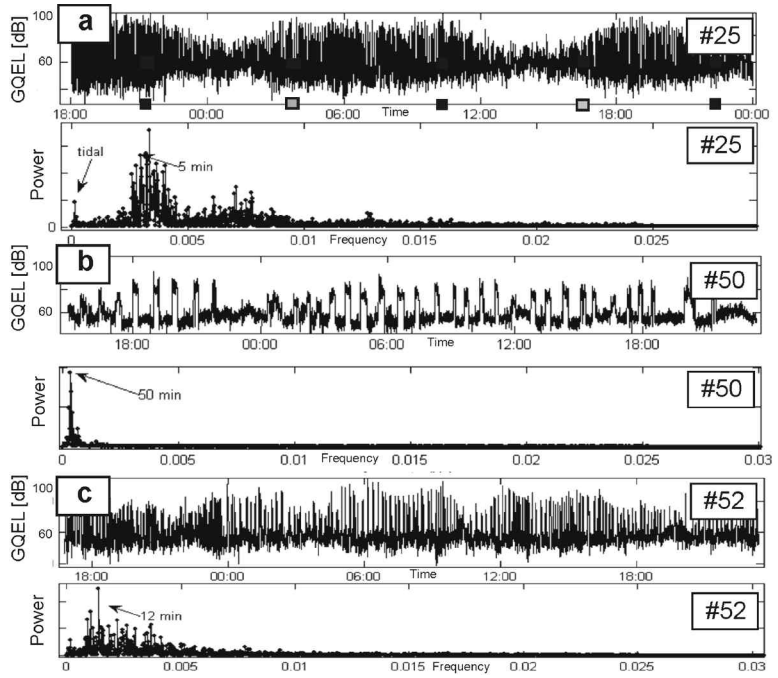

Fig. 9. Stacked trace presentation and the corresponding power spectrum of vent #25 (a), #50 (b), and #52 (c). The cutoff at 0.025 Hz in the frequency domain is caused by previous low-pass filtering.

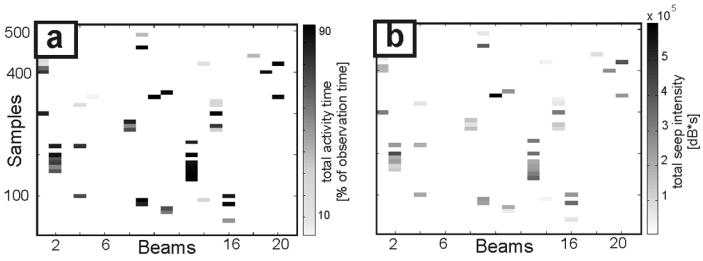

Fig. 10. Spatially distorted top view (*see* Fig. 2) on swath data: (a) distribution of total activity time in percentage of overall observation time and (b) distribution of total seep intensities in absolute values.

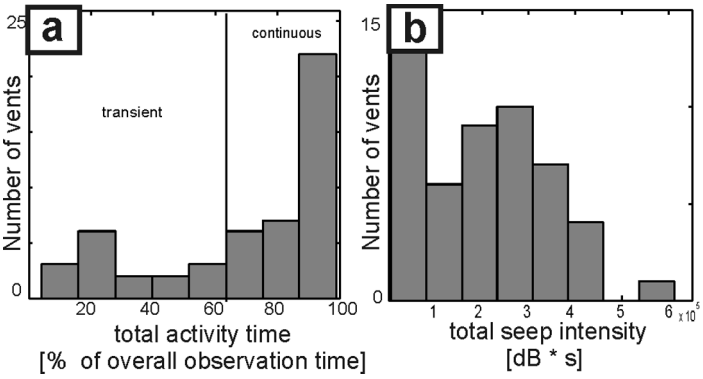

Fig. 11. (a) Eight bin histogram incorporating the total activity time of all seeps. By definition, seeps ≥70% activity are considered continuous (b) eight bin histogram incorporating the total intensity of all seeps.

the context of seepage elsewhere (Wilson et al. 1974; Luyendyk et al. 2003; Artemov et al. 2007).

Considering both histograms in Fig. 11, the question arises if transient vents might emanate as much gas as continuous ones. Short-term periodic gas vents might compensate for their reduced total activity time by more vigorous/stronger seep intensity. For better evaluation, the total seep intensity was normalized by the respective total activity time of each vent and plotted over total activity time, but no trend could be seen. This suggests that short-termed activity is not compensated by increased/very high intensity and that continuously bubbling vents are releasing more gas over long time than noncontinuous vents.

To evaluate the activity of the entire monitored area, all stacked traces were added (GQEL', Fig. 12a) and are plotted together with ADCP volume backscatter *Sv* (Fig. 12b) and/or tidal pressure (Fig. 12c) to see potential interrelations. The maximum tidal range between low and high tide was 0.7 m for the deployment period. A high correlation between the pressure and summed GQEL' exists, where GQEL' lags $\pi/2$ behind the pressure, i.e., the bulk seepage values GQEL' start to increase at the maximum pressure inflection point (Fig. 12a) and peak, when dp/dt drops fastest (Fig. 12c, arrows). The GQEL' values decrease to normal exactly at the pressure minimum. Around 0500 MESZ, the GQEL' shows a slight positive excursion. For the rest of the time, the phase relations between GQEL' and pressure persists. The ADCP *Sv* variable appears to be counter correlated to the stacked traces; this will be discussed later. The absolute ADCP velocity shows no clear correlation to GQEL'.

Compared with previously conducted ROV and submersible surveys for seep inspections (Hovland and Sommerville 1985), the 1.5-fold increased number of seeps per meters squared determined by GasQuant is still in agreement with visual observations. The difference is most likely due to a sampling artifact of time-limited ROV surveys, where episodically active seepage might have simply been missed. Acknowledging this bias, the visually and acoustically determined number of seeps is rather consistent, and we believe that the Tommeliten gas seep area still shows very similar bubble release activities and fluxes as reported two decades ago by Hovland and Judd (1988).

Discussion

External impacts on seep bubble acoustics—

Current effects: The benefits of using water currents for acoustic bubble studies have been presented, however, some disturbing side effects need to be considered. Due to changing currents, the amount of suspended matter in the water may vary and significantly affect scattering of high frequency sources. To evaluate this effect, we used the backscatter data from the ADCP that was simultaneously deployed in the bubble-free environment in the vicinity of the GasQuant lander. With a frequency of 2 MHz, this system is expected to be far more sensitive to suspended particles than GasQuant. However, GQEL' in Fig. 12a were found to be counter-correlated to the ADCP-based backscatter strength *Sv*, and we conclude that the analyzed maximum intensities in the GQEL' (Fig. 12a) are not caused by suspended matter.

Changes in bottom water speed also affect the released bubble size, i.e., enhanced currents support the detaching of bub-

Table 1. Seep classification into continuous (by definition continuous means, that seepage activity is longer than 70 % of observation time) and noncontinuous gas release types.

		Noncontinuous			
		Transient			
Release type	Continuous	Total act. time, <31%	Total act. time, 31% to 50%	Total act. time, 50% to 70%	Purely tidal (on–off)
Number (%)	41 (67%)	7 (11%)	2 (4%)	1 (5%)	1(~1 %)

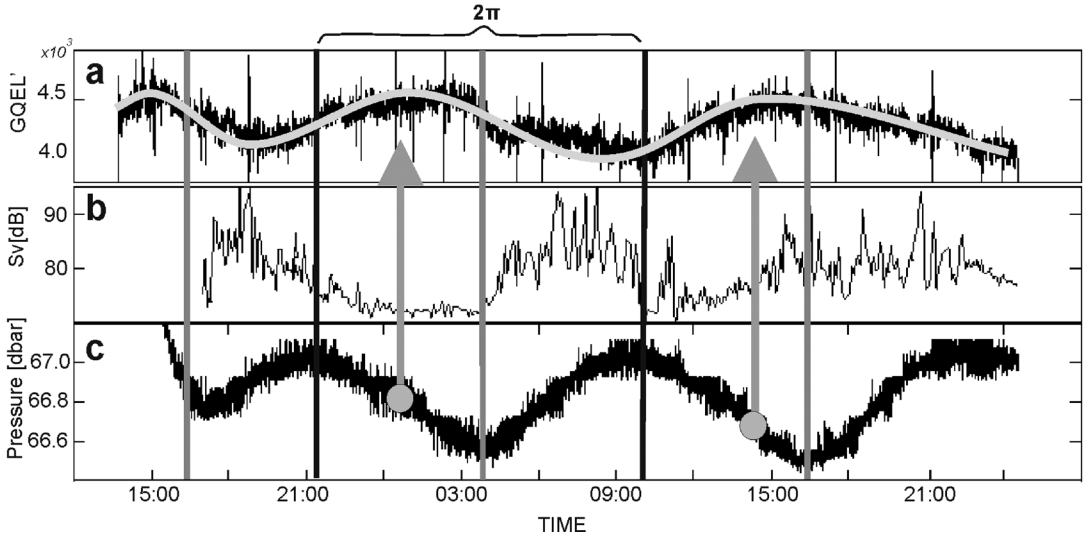

Fig. 12. (a) Time series of summed backscatter values of all seeps (GQEL'), (b) target strength of the ADCP (measured outside the seep area), and (c) the CTD in situ pressure. Varying length of data sets is due to different initialization times of the sensors. Black vertical line indicate high water levels (2π period) separated by low water levels (gray lines). Gray arrows symbolize increased gas flux occurring at the inflection point of pressure decrease. dbar, decibars.

bles from the sediment grain resistance (Leifer pers. comm.) creating smaller bubbles. If the gas flux from below remains constant, a shift of the bubble size spectrum toward smaller radii would increase the amount of bubbles, causing stronger backscatter over time. But no in-phase correlation was seen between current speed and GQEL strength, and current effects are not expected to play an important role here.

Existence of microbubbles: Insonification of resonant microbubbles would rule out the assumed increase between GQEL and gas flux. For the given physical settings, i.e., 180 kHz transmit frequency and 70-m water depth, a resonance radius of 0.05 mm was calculated from Eq. 2. For such small bubbles, the respective rising rate can be calculated with "Stokes law" to be 4 µm/s. For several reasons, the existence of such small microbubbles can be excluded: (1) the sinusoidal displacement pattern would evolve with much stronger amplitude due to slower rise velocity and enhanced time t_{up} to achieve the acoustic swath (Eq. 3). (2) Very slowly rising bubbles would enter and exit the swath gradually; this would result in gently increasing and decreasing values of bursts in trace plots. However, all bubble bursts are characterized by box shapes with steep edges (sudden increase of GQEL). (3) Microbubbles with <0.5 mm radius are too small to rise through consolidated sediment or even to detach from the seafloor because their buoyancy is too small to overcome the resistance of the sediment grains. Microbubbles might form when larger bubbles break up in the water column, but the amount of forming microbubbles is considered to be very small.

Dynamic behavior of gas ebullition—Long-term variation of gas ebullition on a day and month scale are thought to be triggered by tectonic stress, haline, or thermal convection, biological pumping (Tryon et al. 1999), or seasonal temperature fluctuations of the upper seafloor (Wever et al. 2006). Whereas the observed short-term variations within minutes to hours are mainly attributed to tidal- (Martens and Klump 1980; Jackson et al. 1998; Boles et al. 2001), atmospheric- (Mattson and Likens 1990), or swell-induced (Leifer and Boles 2005b) pressure changes, an interplay between varying fluid compositions (oil, tar, and gas: Leifer and Boles 2005a), or the morphological trapping of gas in pockets acting as a short-term reservoir.

Pressure variations crucially affect both the solubility concentration of methane in seawater and the free gas volume. A pressure drop causes more dissolved CH_4 molecules to be transferred to the gaseous phase forcing bubble growth (Leifer and Boles 2005b; "gas charging"). This process is strongest as the pressure drops fastest (dp/dt = min). Furthermore, at the sediment water interface a growing bubble must overcome the overlying hydrostatic pressure. Following the "throat activation" model explained by Boles et al. (2001), a pressure change has immediate impact on the bubble production rate, the lower the hydrostatic pressure the easier a gas bubble will form.

Tidal control: The overall backscatter (GQEL', Fig. 12a) is clearly modulated by a 12-h tidal periodicity. GQEL' values increase as soon as the maximum pressure inflection point is exceeded and peak where the pressure drop is fastest (Fig. 12). The observed π/2 phase lag between maximum pressure and GQEL' indicates gas charging to be responsible for the tidal modulation by pumping dissolved methane out of supersaturated, clay-rich sediment into the gaseous phase. Similar findings, i.e., enhanced gas ebullition triggered at decreasing pressure and peaking at dp/dt = min, have previously been reported by Martens and Klump (1980) and Jackson et al. (1998).

In general, care must be taken by linking tides and gas flux. Depending on the free gas distribution within the sediment and its permeability, the tidal load and unload on the seafloor may be propagating with a phase lag growing with depth (Wang et

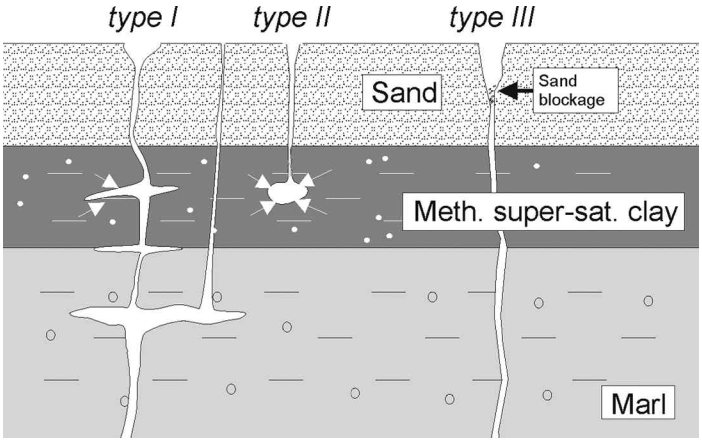

Fig. 13. Schematic sketch of three different gas ebullition types at Tommeliten. Type I is fed from the depth showing interstorage in form of shallow gas pockets; type II is charged in situ from supersaturation of a methane rich layer; and type III proposes direct gas transport in a pipe without local storage and related pocket effects. Meth., method; super-sat., super-saturated.

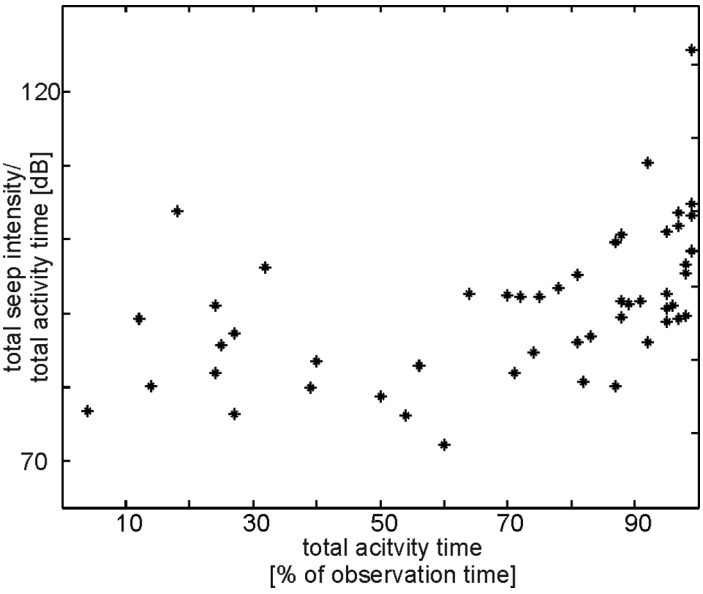

Fig. 14. Comparison of the ratio total seep intensity and total seep activity time, i.e., the averaged burst GQEL for each seep over their activity time percentage. No explicit trend can be discerned.

al. 1998; LaBonte et al. 2007). Because of high permeability and low methane concentrations of the topmost sandy layer, we do not expect such a phase delay to occur in the surficial clay layer. Though, deeper layers may be affected by tidal phase delays.

Mechanical control: Sharp peaks in spectral analysis of the stacked traces (Fig. 9) indicate consistency in periodic gas ebullitions. We hypothesize a more or less steady methane supply from the depth and the temporal variation of gas release being controlled by the gas migration through the clay layer (Fig. 13). Underneath or within this layer, methane may accumulate in reservoirs of different size and depth

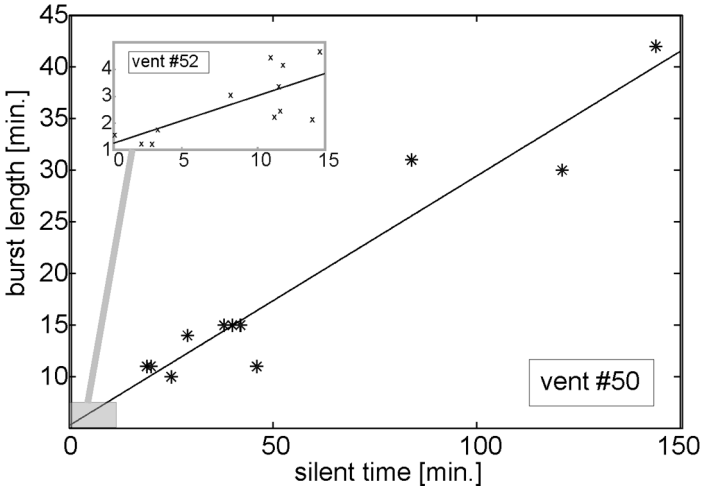

Fig. 15. Relationship between burst length of vent #50 and #52 (subplot) and subsequent length of silent periods. Linear regression yields in both case similar slope values (seep 52: $y = 0.23x + 0.82$; seep 50: $y = 0.24x + 5.3$).

until fracture/pathways open for bubbles to rise into the water column. The pathways remain open until the pressure at pathway throat and the hydrostatic pressure equilibrate. This fracture dominated process, and the resulting on–off character of the vent throat might be compared to single bubble growth processes causing "linear elastic fracture mechanics" described by Boudreau et al. (2005). In contrast, a sandy reservoir responds more plastically to bubble growth giving rise to gently decreasing and increasing bubble growth and fluxes.

The total seep intensity is independent of its activity time (Fig. 14), which indicates that the seeps exhibit on–off characteristics instead of a range of seep intensities. This supports that opening of fractures in elastic/muddy environment controls the flux and not the widening of plastic/sandy pathways. Short periodic venting can also be caused by sand blockage (Fig. 13, type III). This was experimentally verified by Hovland and Sommerville (1985) when they buried an active vent with sand, which then again produced bubbles after 1.5 min. We recognized a 2-min cyclicity in our GasQuant data and propose that the seep surrounding funnel-shaped conduit—as described from ROV surveys—collapses in distinct intervals of a few minutes (maybe due to steepening of the funnel walls) yielding high frequency gas escape patterns.

The burst length of a reservoir-based vent is controlled by the number of moles in the reservoir given by its size and/or internal pressure. As Fig. 15 shows, the longer a silent period, the longer the following bubble burst and vice versa. Moreover, the ratio between active and silent periods of the vents is constant. This supports the idea that the size of reopening fractures, which has an immediate impact on bubble size, is consistent with the gas flux. Fig. 15 depicts a linear relationship between burst length and silent periods covering a wide time range. This

constant ratio between active and silent periods might be a characteristic feature of the Tommeliten seep area and the dominating media (mud/sand). To verify this, data from other locations with other sediment properties are needed.

Comments and recommendations

GasQuant has proven to detect individual gas vents with much higher spatial and temporal resolution than shipborne systems or video observations can offer. The GasQuant multibeam system uses eletronic beamsteering to almost simultaneously insonify the entire monitored area. In contrast, mechanical scanning sonars only monitor each sector only now and then and potentially cause substantial aliasing effects when monitoring gas vents with short bursts.

Compared to optical systems, hydroacoustic systems allow monitoring a larger range and this even in muddy water. The 180 kHz approach has the potential to monitor several hundred meters, although the GasQuant range was system specifically limited to 65 m due to computational constraints in 2001. Improved digital signal processing units and enhanced data mass storage, these days would allow for a much wider range (up to 200 m as at this distance much of the energy would be mainly backscattered from the seafloor) and quicker ping rates (faster than 1 s is not needed as each bubble would be at least insonified 4 times).

GasQuant can be deployed down to 1000 m, and thus, covers the majority of potential seep areas, i.e., the continental margins and slopes. Even within the gas hydrate stability field (below ~500 m), where mechanical gas bubble fluxmeters may fail due to clogging, the hydroacoustic approach is feasible.

Conventional time-consuming shipborne surveys for free gas and seep detection suffer a principle resolution decrease with depth. In contrast, the in situ employment of GasQuant mitigates this problem, and individual vents only decimeters apart from each other can be resolved even at large depths. Thus the system offers a new insight into mid-water-depth seep research. With other more pressure-resistant transducers, such studies could be performed in even greater water depth. However, the deeper the seep site, the more bubble resonance effects there are to be considered.

We suggest performing water current measurements prior to deployments. This will help to orient the system with respect to the targeted seep area in such a way that bubbles move toward and away from the transducer, producing a very distinct bubble pattern in the data. The highest resolution is reached when bubbles move along track the acoustic axes. Relatively short pulses and high ping rates will allow high resolution monitoring of these movements. The typical sinusoidal bubble patterns even evolve at very low water current speed changes that are likely to occur even in the deep open oceans due to tidal influences.

Considering this, bubble displacement could help to design effective cross-correlation bubble detection algorithms (e.g., Particle Imaging Velocimetry) viable for seep research or leakage detection/monitoring. This becomes more important when thinking about using the new generation of water column scanning multibeam sounders for an advanced GasQuant system. Such systems would require automated bubble detection and data reduction techniques to handle the large amount of data. This would be even more important if such a system is deployed as permanent subsea installations to mitigate data transfer limitations. Currently, multi-ping multibeam sounders enter the market that produce two or even three spatially separated acoustic swaths within one transmission cycle. The proposed technique could be improved by relating bubble patterns from one swath with the other and thus reducing the risk of false seep identification.

As we show, the presented multibeam approach for studying bubble release results in a continuous data set where currents help to identify rising bubbles and differentiate them from other backscatterers. For long-term monitoring as part of cabled-observatorier, multibeam systems, such as GasQuant, should be chosen over scanning sonars. They will help to understand the site-specific internal and external factors that modulate the bubble release much better than we are able to do so at the moment.

References

Anderson, V. C. 1950. Sound scattering from a fluid sphere. J. Acoust. Soc. Am. 22:426-431 [doi:10.1121/1.1906621].

Artemov, Y. G., V. N. Egorov, G. G. Polikarpov, and S. B. Gulin. 2007. Methane emission to the hydro- and atmosphere by gas bubble streams in the Dnieper paleo-delta, the Black Sea. Rep. Natl. Acad. Sci. Ukraine 5:110-116.

Boles, J. R., J. F. Clark, I. Leifer, and L. Washburn. 2001. Temporal variation in natural methane seep rate due to tides, Coal Oil Point area, California. J. Geophys. Res. 106:77-86 [doi:10.1029/2000JC000774].

Boudreau, B. P., and others. 2005. Bubble growth and rise in soft sediments. Geology 33:517-520 [doi:10.1130/G21259.1].

Clift, R., J. R. Grace, and M. E. Weber. 1978. Bubbles, drops, and particles. Academic Press.

Commander, K. W., and E. Moritz. 1989. Off-resonance contributions to acoustical bubble spectra. J. Acoust. Soc. Am. 85:2665-2669 [doi:10.1121/1.397763].

D'heur, M. 1984. Porosity and hydrocarbon distribution in the North Sea Chalk Reservoirs. Mar. Pet. Geol. 1:211-238 [doi:10.1016/0264-8172(84)90147-8].

Dworski, J. G., and D. R. Jackson. 1994. Spatial and temporal variation of acoustic backscatter in the STRESS experiment. Cont. Shelf Res. 14:382-390 [doi:10.1016/0278-4343(94)90035-3].

Feuillade, C., and C. S. Clay. 1999. Anderson (1950) revisited. J. Acoust. Soc. Am. 106:553-564 [doi:10.1121/1.427025].

Fofonoff, N. P., and R. C. Millard Jr. 1983. Algorithms for computation of fundamental properties of seawater. Unesco Division of Marine Sciences. Report nr 44. <http://ioc-unesco.org/>. Unesco technical papers in marine science.

Foote, K. G. 1983. Linearity of fisheries acoustics with addition theorems. J. Acoust. Soc. Am. 73:1932-1940 [doi:10.1121/1.389583].

Forster, P., and others. 2007. Changes in atmospheric constituents and in radiative forcing. *In* S. Solomon and others, [eds.], Climate change 2007: The physical science basis: Contribution of Working Group I to the Fourth Assessment Report of the Intergovernmental Panel on Climate Change. Cambridge Univ. Press. Intergovernmental Panel on Climate Change (IPCC) publication.

Greinert, J., and B. Nützel. 2004. Hydroacoustic experiments to establish a method for the determination of methane bubble fluxes at cold seeps. Geo. Mar. Lett. 24:75-85 [doi:10.1007/s00367-003-0165-7].

———, Y. Artemov, V. Egorov, M. De Batist, and D. McGinnis. 2006. 1300-m-high rising bubbles from mud volcanoes at 2080m in the Black Sea: Hydroacoustic characteristics and temporal variability. Earth Planet. Sci. Lett. 244:1-15 [doi:10.1016/j.epsl.2006.02.011].

———. 2008. Monitoring temporal variability of bubble release at seeps: The hydroacoustic swath system GasQuant. J. Geophys. Res. 113:C07048 [doi:10.1029/2007JC004704].

———, D. F. McGinnis, L. Naudts, P. Linke, and M. De Batist. 2009. Spatial methane-bubble flux quantification from seeps into the atmosphere on the Black Sea shelf. J. Geophys. Res. Oceans [doi:10.1029/2009JC005381].

Hornafius, J. S., Q. Derek, and B. P. Luyendyk. 1999. The world's most spectacular marine hydrocarbon seeps (Coal Oil Point, Santa Barbara Channel, California): Quantification of emissions. J. Geophys. Res. 104:20703-20712 [doi:10.1029/1999JC900148].

Hovland, M. 2002. On the self-sealing nature of marine seeps. Cont. Shelf Res. 22:2387-2394 [doi:10.1016/S0278-4343(02)00063-8].

———, and J. M. Sommerville. 1985. Characteristics of two natural gas seepages in the North Sea. Mar. Petrol. Geol. 2:319-326 [doi:10.1016/0264-8172(85)90027-3].

———, and A. G. Judd. 1988. Seabed pockmarks and seepages. Graham and Trotman.

Jackson, D. R., K. L. Williams, T. F. Wever, C. T. Friedrichs, and L. D. Wright. 1998. Sonar evidence for methane ebullition in Eckernförde Bay. Cont. Shelf Res. 18:1893-1915 [doi:10.1016/S0278-4343(98)00062-4].

Judd, A., G. Davies, J. Wilson, R. Holmes, G. Baron, and I. Bryden. 1997. Contributions to atmospheric methane by natural seepage on the U.K. continental shelf. Mar. Geol. 140:427-455 [doi:10.1016/S0025-3227(97)00067-4].

Judd, A. G., and M. Hovland. 2007. Seabed fluid flow. Cambridge Univ. Press [doi:10.1017/CBO9780511535918].

Klaucke, I., H. Sahling, D. Bürk, W. Weinrebe, and G. Bohrmann. 2005. Mapping deep-water gas emissions with sidescan sonar. EOS 86:341-352 [doi:10.1029/2005EO380002].

L-3 ELAC Nautik. 2003. Shallow and medium water multibeam SeaBeam 1000. [Publisher same as author]. Technical handbook 44 301 8004 E.

LaBonte, A. L., K. M. Brown, and M. D. Tryon. 2007. Monitoring periodic and episodic flow events at Monterey Bay seeps using a new optical flow meter. J. Geophys. Res. 112:B02105 [doi:10.1029/2006JB004410].

Leifer, I., J. Boles, B. P. Luyendyk, and J. F. Clark. 2004. Transient discharges from marine hydrocarbon seeps: spatial and temporal variability. Environ. Geol. 46:1038-1052 [doi:10.1007/s00254-004-1091-3].

———, and ———. 2005a. Measurement of marine hydrocarbon seep flow through fractured rock and unconsolidated sediment. Mar. Petrol. Geol. 22:551-568 [doi:10.1016/j.marpetgeo.2004.10.026].

———, and ———. 2005b. Turbine tent measurements of marine hydrocarbon seeps on subhourly timescales. J. Geophys. Res. 109:1-12.

———, and ———. 2006. Corrigendum to: Measurement of marine hydrocarbon seep flow through fractured rock and unconsolidated sediment: [Marine and Petroleum Geology 22 (2005), 551–558]. Mar. Petrol. Geol. 23:401 [doi:10.1016/j.marpetgeo.2006.02.006].

Lelieveld, J., P. J. Crutzen, and C. Brühl. 1993. Climate effects of atmospheric methane. Chemosphere 26:739-768 [doi:10.1016/0045-6535(93)90458-H].

Luyendyk, B. P., L. Washburn, S. Banerjee, J. F. Clark, and D. C. Quigley. 2003. A methodology for investigation of natural hydrocarbon gas seepage in the Northern Santa Barbara Channel. Coastal Research Center, Marine Science Institute, University of California, Santa Barbara, CA. MMS OCS Study 2003-054. MMS Cooperative Agreement Number 14-35-0001-30758.

MacDonald, I. R., N. L. Guinasso Jr., R. Sassen, J. M. Brooks, L. Lee, and K. T. Scott. 1994. Gas hydrate that breaches the sea floor on the continental slope of the Gulf of Mexico. Geology 22:699-702 [doi:10.1130/0091-7613(1994)022<0699:GHTBTS>2.3.CO;2].

Martens, C. S., and J. V. Klump. 1980. Biogeochemical cycling in an organic-rich coastal marine basin - I. Methane sediment-water exchange processes. Geochim. Cosmochim. Acta 44:471-490 [doi:10.1016/0016-7037(80)90045-9].

Mattson, M. D., and G. E. Likens. 1990. Air pressure and methane fluxes. Nature. 347:718-719 [doi:10.1038/347718b0].

McCartney, B. S., and B. M. Bary. 1965. Echo-sounding on probable gas bubbles from the bottom of Saanich Inlet, British Columbia. Deep Sea Res. 12:285-294.

Medwin, H. 1977. Acoustical determinations of bubble-size spectra. J. Acoust. Soc. Am. 62:1041-1044 [doi:10.1121/1.381617].

Merewether, R., M. S. Olsson, and P. Lonsdale. 1985. Acoustically detected hydrocarbon plumes rising from 2-km Depths in Guaymas Basin, Gulf of California. J. Geophys. Res. 90:3075-3085 [doi:10.1029/JB090iB04p03075].

Minnaert, M. 1933. On musical air bubbles and the sounds of running water. Philos. Mag. 10:235-248.

Niemann, H., and others. 2005. Methane emission and consumption at a North Sea gas seep (Tommeliten area). Biogeosciences 2:335-351.

Nikolovska, A., H. Sahling, and G. Bohrmann. 2008. Hydroacoustic methodology for detection, localization, and quantification of gas bubbles rising from the seafloor at gas seeps from the eastern Black Sea. Geochem. Geophys. Geosyst. 9:Q10010 [doi:10.1029/2008GC002118].

Ohle, W. 1960. Fernsehen, Photographie und Schallortung der Sedimentoberfläche in Seen. Arch. Hydrobiol. 57:135-160.

Ostrovsky, I., D. Mcginnis, L. Lapidus, and W. Eckert. 2008. Quantifying gas ebullition with echosounder: the role of methane transport by bubbles in a medium-sized lake. Limnol. Oceanogr. Methods 6:105-118.

Pfannkuche, O., and P. Linke. 2003. GEOMAR landers as long-term deep-sea observatories. Sea Technol. 44:50-55.

Rehder, G., R. S. Keir, E. Suess, and T. Pohlmann. 1998. The multiple sources and patterns of methane in North Sea Waters. Aquatic Geochem. 4:403-427 [doi:10.1023/A:1009644600833].

———, P. W. Brewer, E. T. Peltzer, and G. Friederich. 2002. Enhanced lifetime of methane bubble streams within the deep ocean. Geophys. Res. Lett. 29 [doi:10.1029/2001GL013966].

Sauter, E. J., and others. 2006. Methane discharge from a deep-sea submarine mud volcano into the upper water column by gas hydrate-coated methane bubbles. Earth Planet. Sci. Lett. 243:354-365 [doi:10.1016/j.epsl.2006.01.041].

Schneider von Deimling, J., J. Brockhoff, and J. Greinert. 2007. Flare imaging with multibeam sonar systems: Data processing for seep bubble detection. Geochem. Geophys. Geosyst. 8:1-7 [doi:10.1029/2007GC001577].

Tryon, M. D., K. M. Brown, M. E. Torres, A. M. Tréhu, J. McManus, and R. W. Collier. 1999. Measurements of transience and downward fluid flow near episodic methane gas vents, Hydrate Ridge, Cascadia. Geology 27:1075-1078 [doi:10.1130/0091-7613(1999)027<1075:MOTADF>2.3.CO;2].

———, ———, and ———. 2002. Fluid and chemical flux in and out of sediments hosting methane hydrate deposits on Hydrate Ridge, OR, II: Hydrological processes. Earth Planet. Sci. Lett. 201:541-557 [doi:10.1016/S0012-821X(02)00732-X].

Vagle, S., and D. M. Farmer. 1992. The measurement of bubble-size distributions by acoustical backscatter. J. Atmos. Ocean. Technol. 9:630-644 [doi:10.1175/1520-0426(1992)009<0630:TMOBSD>2.0.CO;2].

Wang, K., E. E. Davis, and G. Van Der Kamp. 1998. Theory for the effect of free gas in subsea formations on tidal pore pressure variations and seafloor displacements. J. Geophys. Res. 103:339-353 [doi:10.1029/98JB00952].

Wever, T. F., R. Lühder, H. Voß, and U. Knispel. 2006. Potential environmental control of free shallow gas in the seafloor of Eckernförde Bay, Germany. Mar. Geol. 225:1-4 [doi:10.1016/j.margeo.2005.08.005].

Wilson, R. D., P. H. Monaghan, A. Osanik, L. C. Price, and M. A. Rogers. 1974. Natural marine oil seepage. Science 184:857-865 [doi:10.1126/science.184.4139.857].

Submitted 12 May 2009
Revised 23 November 2009
Accepted 4 December 2009